







## *In situ* investigation of the ferroelectric phase transition in improper ferroelectric YMnO<sub>3</sub> thin films by electron energy loss spectroscopy

Alexander Vogel <sup>1,2</sup>, Alicia Ruiz-Caridad <sup>1</sup>, Johanna Nordlander <sup>2,3</sup>, Rolf Erni <sup>1,2</sup>,  
Morgan Trassin <sup>2</sup> and Marta D. Rossell <sup>1</sup>

<sup>1</sup>*Electron Microscopy Center, Empa, Swiss Federal Laboratories for Materials Science and Technology, Dübendorf CH-8600, Switzerland*

<sup>2</sup>*Department of Materials, Eidgenössische Technische Hochschule Zürich, Zürich CH-8092, Switzerland*

<sup>3</sup>*Department of Physics, Harvard University, Cambridge, Massachusetts 02138, USA*



(Received 13 March 2023; accepted 5 June 2023; published 21 June 2023)

The crystal and electronic structure of YMnO<sub>3</sub> thin films at the paraelectric-ferroelectric phase transition are monitored by scanning transmission electron microscopy and electron energy loss spectroscopy (EELS) during *in situ* heating experiments. At the phase transition of a 14-unit-cell-thick film at  $\sim 325^\circ\text{C}$ , we observe a clear transition from the polar  $P6_3cm$  to the centrosymmetric  $P6_3/mmc$  space group, manifested by the disappearance of the unit-cell tripling. Further, we reveal significant changes in the EELS data across the phase transition, and interpret them with the help of real-space multiple-scattering calculations. Upon crossing the Curie temperature, striking changes in the O-K near-edge structure are identified, which are attributed to a modification in the Y 4d–O 2p hybridization. In particular, a weakening of the Y 4d<sub>z<sup>2</sup></sub>–O 2p<sub>z</sub> hybridization is detected for the paraelectric phase compared to the ferroelectric phase. Upon cooling below the Curie temperature, the ferroelectric phase is recovered and a stronger hybridization along the *c*-axis polarization direction is restored, stabilizing the zone-boundary K<sub>3</sub> phonon mode. Our findings demonstrate the high sensitivity of the O-K near-edge structure to structural distortions in YMnO<sub>3</sub> polymorphs and lay the groundwork for future studies on polymorphic phase transformations in improper ferroelectrics whose ferroelectricity emerges through coupling to a nonpolar lattice distortion.

DOI: [10.1103/PhysRevB.107.224107](https://doi.org/10.1103/PhysRevB.107.224107)

### I. INTRODUCTION

The functional properties of many materials are closely linked to symmetry-changing phase transitions. Examples include ferroelectric polarization, ferromagnetic magnetization, multiferroicity, second-harmonic generation, nonreciprocity, various Hall-effect-type transport properties, and many others [1]. In particular, many perovskite materials undergo a temperature-driven phase transition at the so-called Curie temperature ( $T_c$ ) from a nonpolar paraelectric phase at high temperature to a lower-temperature, noncentrosymmetric polar ferroelectric phase. The spontaneous polarization that ferroelectric materials exhibit below this transition temperature has made them promising candidates for nonvolatile memories [2,3]. In *improper* ferroelectrics, the phase transition is governed by a primary order parameter, such as a structural distortion [4–6] or a magnetic spin alignment [7], which is independent of electrostatics and the ferroelectric polarization arises as a secondary effect of this order parameter. As a result, in contrast to *proper* ferroelectrics, the ferroelectric properties of improper ferroelectrics are expected to be robust against the detrimental effects of the depolarizing field [8], which is important for the continued miniaturization of ferroelectric devices, down to the ultrathin limit.

Of the various known improper ferroelectrics, hexagonal manganites (*h*-RMnO<sub>3</sub>, *R* = rare earth) have attracted much attention due to their multiferroic properties, vortex-antivortex topological domain configurations, conducting domain walls, magnetoelectric coupling, and even as a model system to

study the Kibble-Zurek mechanism [9–19]. In particular, YMnO<sub>3</sub> (YMO) is the most investigated material of the *h*-RMnO<sub>3</sub> class. In its paraelectric phase, it crystallizes in the centrosymmetric  $P6_3/mmc$  space group, consisting of corner-sharing MnO<sub>5</sub> bipyramids alternating with Y<sup>3+</sup> ion layers along the *c* axis [6]. A structural phase transition to the noncentrosymmetric  $P6_3cm$  space group occurs at a  $T_c$  of  $\sim 997^\circ\text{C}$  when the unit cell triples as a result of a zone-boundary K<sub>3</sub> phonon-mode condensation [6]. In this structure, the Mn cation is surrounded by two apical O ions (O1,2) and three planar O ions (one O3 and two O4), while the Y cation is coordinated by eight O ions, as depicted in Fig. 1. The lattice trimerizing distortion is driven by a tilt of the MnO<sub>5</sub> bipyramids around the Y<sup>3+</sup> ions and a buckling of the Y layers [6,20]. In Figs. 1(a)–1(c), an outward tilt of the MnO<sub>5</sub> bipyramids is illustrated, and the Y1 ion is displaced downwards relative to the Y2 ions. The ferroelectric polarization arises due to the coupling of a polar  $\Gamma_2^-$  mode, consisting of a shift of the Y layer towards the MnO layer. Commonly, the trimerization is described by a two-component order parameter **Q** consisting of the tilt amplitude *Q* and the azimuthal tilt angle  $\varphi$  of the MnO<sub>5</sub> bipyramids [21]. In Fig. 1(c), **Q** and  $\varphi$  are defined, as seen along the [001] axis. In addition, it can also be related to the amplitude of the corrugation of the Y-ion layers and their phase (the different up/down displacement patterns of the Y ions) [17]. In this case, **Q** refers to the amplitude of a sinusoidal function that is fitted to the Y-ion positions and  $\varphi$  to its phase, as illustrated in Fig. 1(a). Finally, a change in the Y–O bond distances is observed at the

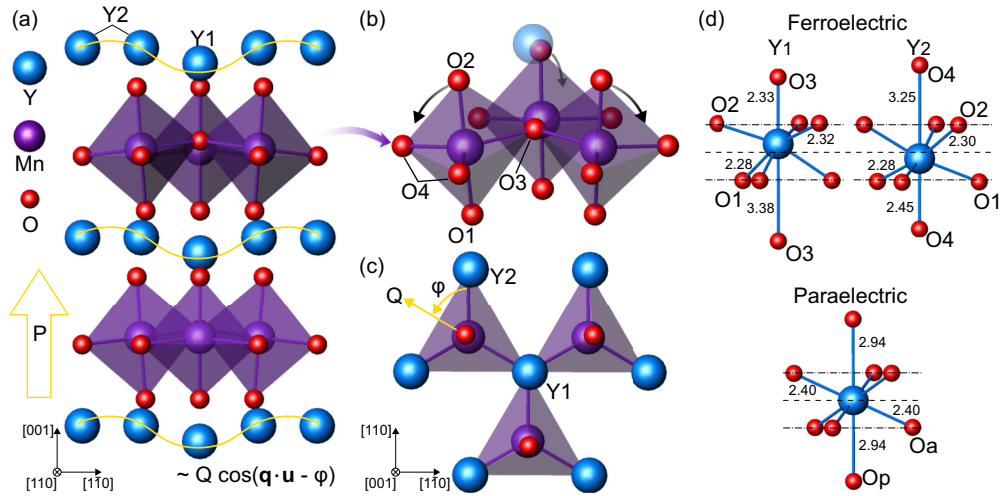


FIG. 1. Schematics of the ferroelectric  $\text{YMnO}_3$  crystal structure with  $P6_3cm$  space group. (a) View along the  $[110]$  axis. The polarization  $P$  and the sinusoidal corrugation of the Y-ion layers is indicated and the relation to the trimerization parameter  $Q$  is given. (b) Enlarged view of the  $\text{MnO}_5$  trigonal bipyramids highlighting the rotation of the polyhedra. The two apical oxygen positions (O1,2) and three planar oxygen positions (O3,4) are labeled. (c) View along the  $[001]$  crystal direction. The tilt amplitude  $Q$  and azimuthal tilt angle  $\varphi$  are given. (d) Enlarged view of the  $\text{YO}_8$  cages in the ferroelectric (top) and paraelectric (bottom) phases. The oxygen positions are labeled and the bond distances are given for both phases. The bond distances of the paraelectric phase were calculated using the lattice expansion measured from the HAADF-STEM images.

paraelectric-ferroelectric (PE-FE) phase transition. The bond lengths for the two inequivalent Y positions in the ferroelectric phase and for the paraelectric phase are displayed in Fig. 1(d).

Experimental studies on the phase transition in YMO have long reported a structural anomaly between  $527^\circ\text{C}$  and  $T_c$ , leading to a wide range of  $T_c$  values and suggestions of two distinct structural transitions [22–27]. Today it is understood that at  $T_c$  there is a single phase transition and the spontaneous polarization slowly emerges as a secondary effect [6,21,28–31]. In particular, a study by Skjærvø *et al.* revealed that the phase-transition confusion arose from an unconventional order-disorder phase transition [29]. By combining theoretical calculations with neutron diffraction experiments, they showed that local low-symmetry distortions are preserved in the high-symmetry phase. Specifically, below  $527^\circ\text{C}$  the phase of the order parameter undertakes one of the six ground states. Above  $527^\circ\text{C}$ , but still below  $T_c$ , fluctuations smear the local distribution of  $\varphi$  until it spans a continuum of values above  $T_c$ . In addition, the amplitude  $Q$  of the distortion remains distinctly nonzero above the phase transition. This was further confirmed in a recent report by Nordlander *et al.* [32]. Using *in situ* second-harmonic generation, they showed a strong thickness dependence of  $T_c$  in YMO thin epitaxial films with an unexpected critical thickness below 3 unit cells. This finding enabled bringing the phase transition to experimentally accessible temperatures for *in situ* scanning transmission electron microscopy (STEM) imaging studies, and the nonzero amplitude of the Y-ion layer corrugation above  $T_c$  was confirmed.

The exact details of the electronic structure in YMO during the phase transition have however remained unclear to date. Van Aken *et al.* suggested that the Y–O bonds are almost ionic in character and the off-centering is stabilized

by the electrostatic energy alone without contributions from chemical activity such as charge transfer or rehybridization of covalent bonds [20]. However, reports by Cho *et al.* using x-ray absorption spectroscopy [27] and Kim *et al.* using electron density analysis from synchrotron radiation powder diffraction [24] indicated that rehybridization of the Y1–O3,4 bond does occur below  $T_c$ . In particular, a strong anisotropic hybridization was observed not only for Mn  $3d$ –O  $2p$  but also for Y  $4d$ –O  $2p$  bonds [27]. Furthermore, Kumagi *et al.* have demonstrated that a strong covalency in the R–O bond is detrimental to ferroelectricity in  $h$ – $\text{RMnO}_3$  compounds [33], contrary to observations in proper ferroelectrics, such as  $\text{BaTiO}_3$ . Advancing the understanding of the phase-transition mechanisms of the improper ferroelectric model system YMO is key to controlling exotic polarization states and developing emerging ferroelectric-based electronics.

Here, we investigate the electronic structure of  $\text{YMnO}_3$  epitaxial thin films across the PE-FE phase transition by *in situ* heating experiments in the transmission electron microscope. In particular, electron energy loss spectroscopy (EELS) is used to monitor changes in the bonding characteristics and oxidation state by analyzing the O–K and Mn–L edges during heating experiments. Our observations are then interpreted by comparison with theoretical calculations of the O–K edge and the corresponding projected density of unoccupied states.

## II. METHODS

### A. Thin-film growth

The YMO thin films were grown on Pt(111)-buffered  $\text{SrTiO}_3(111)$  substrates by pulsed laser deposition (PLD) using a KrF excimer laser at 248 nm, an energy fluence of  $0.5$ – $0.7\text{J}/\text{cm}^2$ , and a repetition rate of 8 Hz, ablating

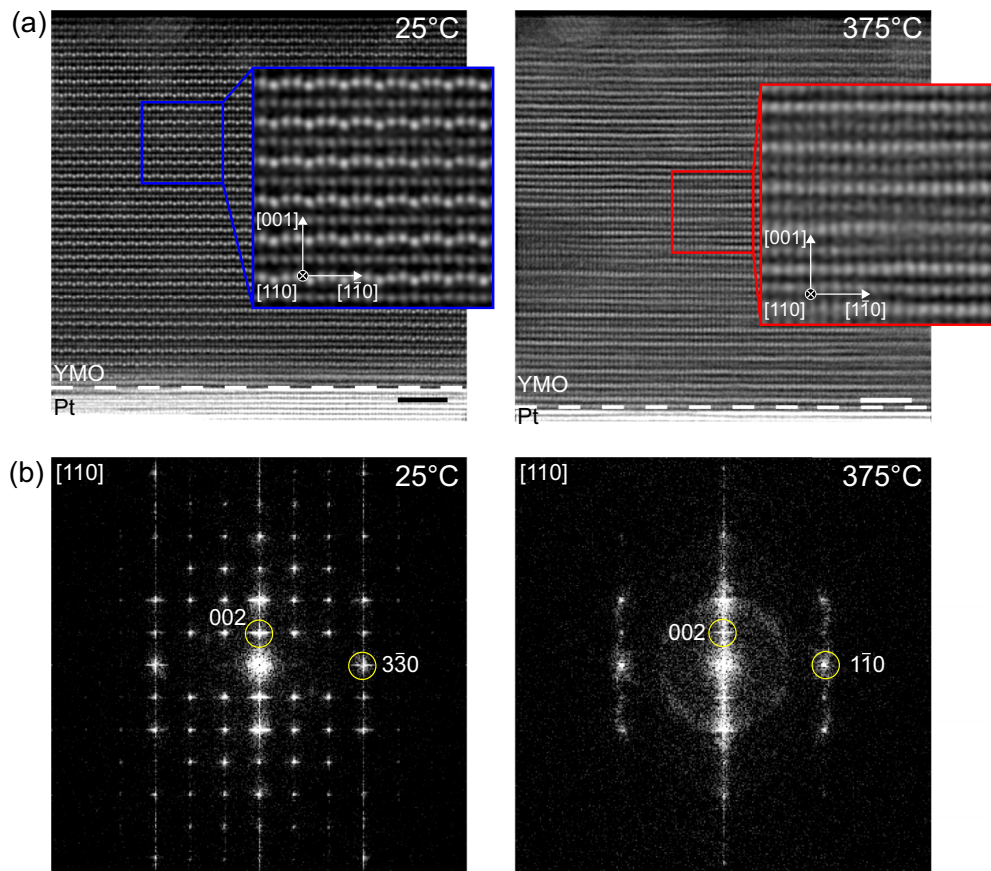


FIG. 2. (a) Representative averaged HAADF-STEM images of a 14-u.c. YMO film recorded at room temperature (left) and 375 °C (right). The images were filtered in Fourier space, using a bandpass filter. The insets show magnified views, highlighting the change in the Y-ion layer corrugation at the paraelectric-ferroelectric phase transition. Scale bars are 2 nm. (b) Corresponding Fourier transforms. The crystallographic directions are given and the diffraction spots are indexed. The loss of the superlattice reflections at high temperature is a clear indication of trimerization loss.

from a stoichiometric  $\text{YMnO}_3$  target [34]. The Pt buffer was deposited by magnetron sputtering on a Ti adhesion layer. The Pt and Ti layers were deposited at 700 °C in 0.05-mbar Ar plasma during 15 min and 50 s at a power of 10 and 20 W, respectively. After the buffer deposition, the sample was transferred *in situ* directly to the PLD chamber. During the YMO thin-film deposition, the substrate was kept at 800 °C in 0.12-mbar  $\text{O}_2$  environment. The thickness of the thin films was monitored using reflection high-energy electron diffraction during growth and cross checked with postdeposition x-ray reflectivity.

### B. Scanning transmission electron microscopy

Electron transparent samples for STEM investigations were prepared in cross-section geometry by using an FEI Helios 660 G3 UC focused ion beam operated at acceleration voltages of 30 and 5 kV after deposition of C and Pt protective layers. An FEI Titan Themis operated at 300 kV and equipped with a probe CEOS DCOR spherical aberration corrector and a CEFID (CEOS Energy Filtering and Imaging Device) spectrometer [35,36] retrofitted with a hybrid-pixel ELA detector from Dectris Ltd. [37] was used for high-angle annular dark-field scanning transmission electron microscopy

(HAADF-STEM) imaging and EELS. For HAADF-STEM, a probe semiconvergence angle of 18 mrad was set in combination with an annular semidetector range of 66–200 mrad for the annular dark-field detector. The EELS data were obtained by setting the convergence and collection semiangles to 26 and 35 mrad, respectively, yielding an effective collection semiangle of about 29.5 mrad for the inspected energy loss range. The O-K and Mn-L edges were acquired jointly with a dispersion of 0.19 eV per channel. The *in situ* heating experiments were performed using a heating rate of 5 °C/s from room temperature (25 °C) to 425 °C. EELS data were collected at selected temperatures, where the temperature was held for approximately 1 min to allow thermal drift of the sample to subside. Afterwards, the specimen was cooled down at a cooling rate of 5 °C/s back to room temperature. This heating-cooling cycle was repeated four times.

### C. Data processing and analysis

The averaged HAADF-STEM images displayed in Fig. 2 were obtained after nonrigid registration of time series consisting of 12 frames ( $2048 \times 2048$  pixels at a dwell time of 1  $\mu\text{s}$ ) using the [38] software. The obtained images were filtered in Fourier space using a bandpass filter.



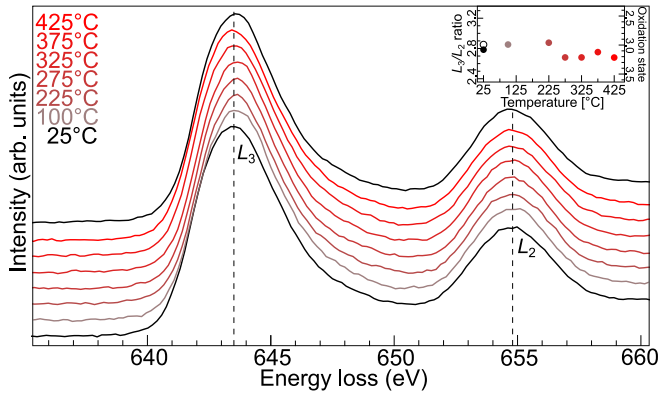


FIG. 3. Mn- $L_{3,2}$  edge EEL spectra of a 14-u.c. YMO film at various temperatures. The inset shows the integrated Mn  $L_3/L_2$  intensity ratio for the different temperatures and the corresponding Mn oxidation state. The solid and open black circles show the values of the Mn  $L_3/L_2$  intensity ratio before and after the heating cycle, respectively.

The Mn- $L_{3,2}$  and O- $K$  edge spectra displayed in Figs. 3–5 were acquired from the center of the YMO film at different temperatures, to ensure no contributions from interface regions. The background signal was subtracted by fitting a power-law function to an energy window of  $\sim 60$  eV before the Mn- $L_{3,2}$  edge onset. The spectra were then normalized to the  $L_2$ -edge intensity. The Mn  $L_3/L_2$  intensity ratio, displayed in the inset of Fig. 3, was obtained by integrating the intensity of the  $L_3$  and  $L_2$  edges after subtracting the contributions of the continuum orbitals using a Hartree-Slater cross-section function. For the O- $K$  edge spectra displayed in Figs. 4 and 5, a power-law background subtraction was performed following the same procedure as for the Mn- $L_{3,2}$  edge and the spectra were finally normalized to the intensity of the  $b$  peak.

#### D. Simulations

The real-space multiple-scattering code FEFF 9.6 [39] was used for the calculation of the energy loss near-edge structures

(ELNES) of the O- $K$  edge as well as the projected density of states (PDOS) of the  $h$ -YMO polar ferroelectric phase with the noncentrosymmetric  $P6_3cm$  space group. The EEL spectra were computed taking into account the same convergence and collecting semiangles and crystallographic orientations as the experiments. The scattering potentials were calculated self-consistently over a radius of  $5.5 \text{ \AA}$  using Hedin-Lundqvist (local density approximation) self-energies [40]. For the full multiple-scattering (FMS) calculations, the calculations converged for clusters as small as 144 atoms. Hence, the spectra and projected density-of-state (PDOS) calculations presented here were all modeled for 144 atoms in the FMS cluster. In addition, 14 self-consistent iterations were necessary to converge the total and projected density of states from the FEFF calculations and we followed the procedure described in Ref. [41], including an additional shift of about 3 eV in the Fermi energy to match the experimental evidence of a band gap in the material.

### III. RESULTS

To begin with, the structural phase transition of a 14 unit-cell (u.c.)-thick YMO film was determined by *in situ* heating TEM. We imaged the structural distortion in real space using atomic-resolution HAADF-STEM imaging while heating the YMO film *in situ*. As expected, the FE  $\rightarrow$  PE phase transition took place at a much lower temperature than the bulk  $T_c \approx 997^\circ\text{C}$  [32,42]. In particular, we observe an apparent structural phase transition at  $\sim 350^\circ\text{C}$ . In Fig. 2(a), two representative HAADF-STEM images recorded at room temperature (left) and  $375^\circ\text{C}$  (right) are displayed. The magnified view of the room-temperature image clearly shows the trimerized lattice recognized by its characteristic “up-up-down” displacement pattern of Y atoms parallel to  $[001]$ . In contrast, the Y-ion layer corrugation is absent in the image recorded at  $375^\circ\text{C}$ . This is supported by the corresponding Fourier transforms in Fig. 2(b). Here, the loss of the superlattice reflections upon heating the film is a clear indication of symmetry change. Note that the image quality at elevated temperatures is notably worse than at room temperature. This is partly due to thermal expansion of the supporting ceramic

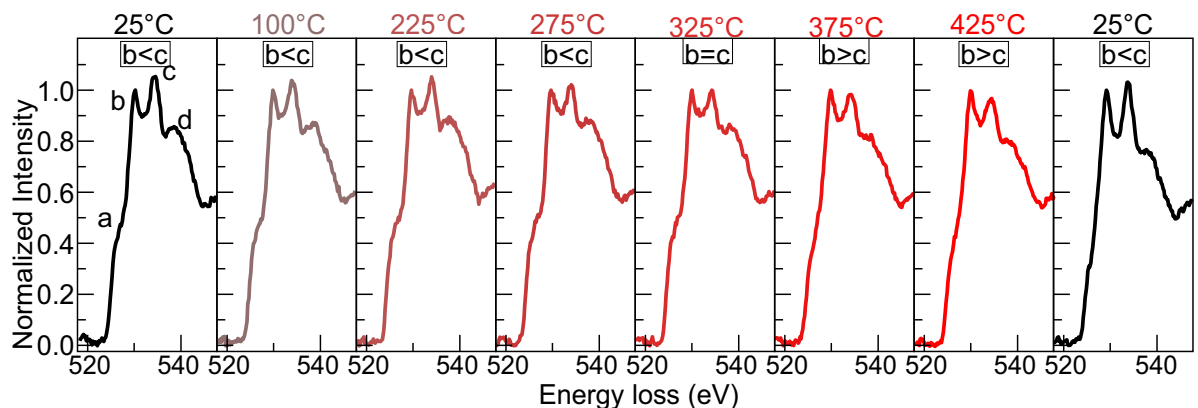


FIG. 4. O- $K$  edge EEL spectra of a 14-u.c. YMO film at increasing temperatures. The relative intensity for peaks  $b$  and  $c$  is indicated. Above  $325^\circ\text{C}$ , the intensity ratio  $b/c$  shifts from  $b < c$  to  $b > c$ . Upon cooling down to room temperature, the peak intensity ratio  $b/c$  returns to  $b < c$ . For clarity, the spectra are normalized to the intensity of the peak  $b$ .

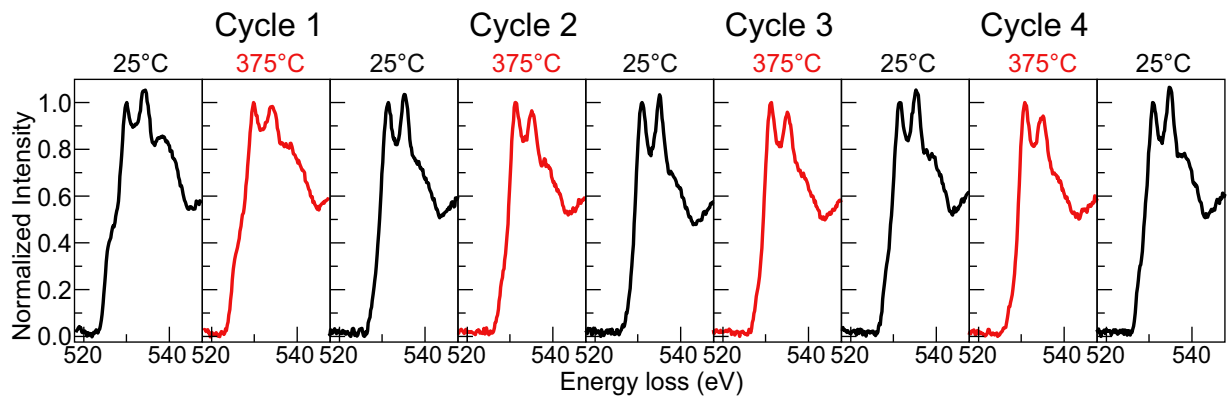


FIG. 5. O-K edge EEL spectra of a 14-u.c. YMO film recorded over four heating cycles. The change in intensity ratio of the *b* and *c* peaks is reproduced over the four cycles. For clarity, the spectra are normalized to the intensity of the peak *b*.

membrane to which the TEM lamella is attached, which manifests as thermal drift and a minor sample mistilt. Furthermore, structural defects, such as stacking faults, form in the YMO thin films if they are kept at high temperatures for a long time. The appearance of these defects after prolonged heating is likely due to the formation of oxygen vacancies, as discussed below. Nevertheless, our *in situ* heating results unequivocally demonstrate that the ferroelectric phase transition of the 14-u.c. YMO film takes place at  $\sim 350^\circ\text{C}$ , in good agreement with previous reports [32,42]. In addition, we detect a thermal expansion of the lattice parameters of the paraelectric phase (at  $375^\circ\text{C}$ ) with respect to the ferroelectric phase (at  $25^\circ\text{C}$ ) of approximately  $4.7 \pm 0.9\%$  and  $3.2 \pm 1.8\%$  in-plane and out-of-plane, respectively.

Next, in order to investigate the electronic structure variations across the improper ferroelectric phase transition, EELS was used to first probe the oxidation state of the manganese ions across the phase transition by probing the Mn- $L_{3,2}$  edge during a single heating cycle from room temperature ( $25^\circ\text{C}$ ) to  $425^\circ\text{C}$ . The results are displayed in Fig. 3. The Mn- $L_{3,2}$  edge corresponds to excitations from the Mn  $2p$  electrons to empty Mn  $3d$  states. In particular, these transitions produce two characteristic features at  $\sim 643$  eV (Mn- $L_3$ ) and  $\sim 655$  eV (Mn- $L_2$ ) due to spin-orbit splitting of the Mn  $2p$  core hole into  $2p_{3/2}$  and  $2p_{1/2}$  states, respectively. Two approaches are typically employed to quantitatively determine the Mn oxidation state from the ELNES of the Mn- $L_{3,2}$  edge: changes in the  $L_3/L_2$  intensity ratio and the position of the edge onset energy [42–45]. From Fig. 3, no significant energy shift of the Mn- $L_{3,2}$  edge is detected during the heating cycle. Further, the analysis of the Mn- $L_3/L_2$  intensity ratio (shown in the inset of Fig. 3) reveals only minimal variations in the  $L_3/L_2$  intensity ratio around 2.8, indicating a stable  $\text{Mn}^{3+}$  oxidation state through the first heating cycle [42].

Additional information about the electronic structure of YMO across the ferroelectric phase transition can be obtained from the O-K edge spectra of Fig. 4, which were recorded simultaneously with the Mn- $L_{3,2}$  edge spectra displayed in Fig. 3. The O-K edge results from excitations of O  $1s$  core electrons into available O  $2p$  empty states. Thus, the unoccupied states with O  $2p$  character are probed and relevant information about the hybridization of the O  $2p$  states with the

metal orbitals can be obtained [46,47]. At room temperature, we identify four major features (labeled *a–d*) at energy losses of *a*: 526 eV, *b*: 530 eV, *c*: 534 eV, and *d*: 538 eV. Further, we observe significant changes in the intensity ratio of peaks *b* and *c* with increasing temperature. Specifically, peak *c* is more intense than peak *b* below  $325^\circ\text{C}$ . At  $325^\circ\text{C}$ , both peaks are equally intense, whereas at  $375^\circ\text{C}$  and above, the intensity of peak *c* decreases, so that peak *b* becomes more intense than peak *c*. Most importantly, the peak ratio returns to its initial state upon cooling to room temperature. We link the observed O-K edge changes primarily to the PE-FE phase transition, rather than to the formation of oxygen vacancies, as our analysis of the Mn- $L_{3,2}$  edge shows no significant change in the oxidation state of Mn.

To rule out possible artifacts during a single phase transition, we acquired EEL spectra of the O-K edge at  $25^\circ\text{C}$  and  $375^\circ\text{C}$  across several heating-cooling cycles. Figure 5 shows the result of these measurements. It is evident that the change in the intensity ratio of peaks *b* and *c* is reproduced throughout the four cycles and that the original state is restored at the end of the last cycle. Simultaneously, a decrease in the intensity of peak *a* is observed throughout the four cycles. The intensity of peak *a* is not recovered after the last heating cycle. This suggests the formation of oxygen vacancies over the course of multiple heating cycles [48,49].

To interpret the ELNES changes in the O-K edge spectra, we compare our experimental results with theoretical simulations of the O-K edge and the corresponding PDOS of the O  $2p$ , Mn  $3d$ , Y  $4d$ , Mn  $4s$ , and Y  $5s$  states. The calculated O-K edge spectra of the ferroelectric  $\text{YMnO}_3$  phase are shown in Fig. 6 (top). Four main peaks (*a–d*) are observed in this spectrum, consistent with our experimental data. To assign the spectral features to transitions to specific electronic states, the corresponding calculated PDOS are plotted below. Thus, we find that peak *a* mostly stems from transitions to hybridized O  $2p$ -Mn  $3d$  orbitals. Peak *b* arises from hybridization of O  $2p$  states with Mn  $3d$  states as well as some Y  $4d$ , Mn  $4s$ , and Y  $5s$  states. Peak *c* is identified as hybridized O  $2p$  and Y  $4d$  states, while peak *d* corresponds to O  $2p$  states hybridized with Mn  $4s$  and Y  $5s$  states. Hence, we can attribute the evolution of the EEL spectra to a Y  $4d$ -O  $2p$  rehybridization at the PE  $\rightarrow$  FE phase transition.

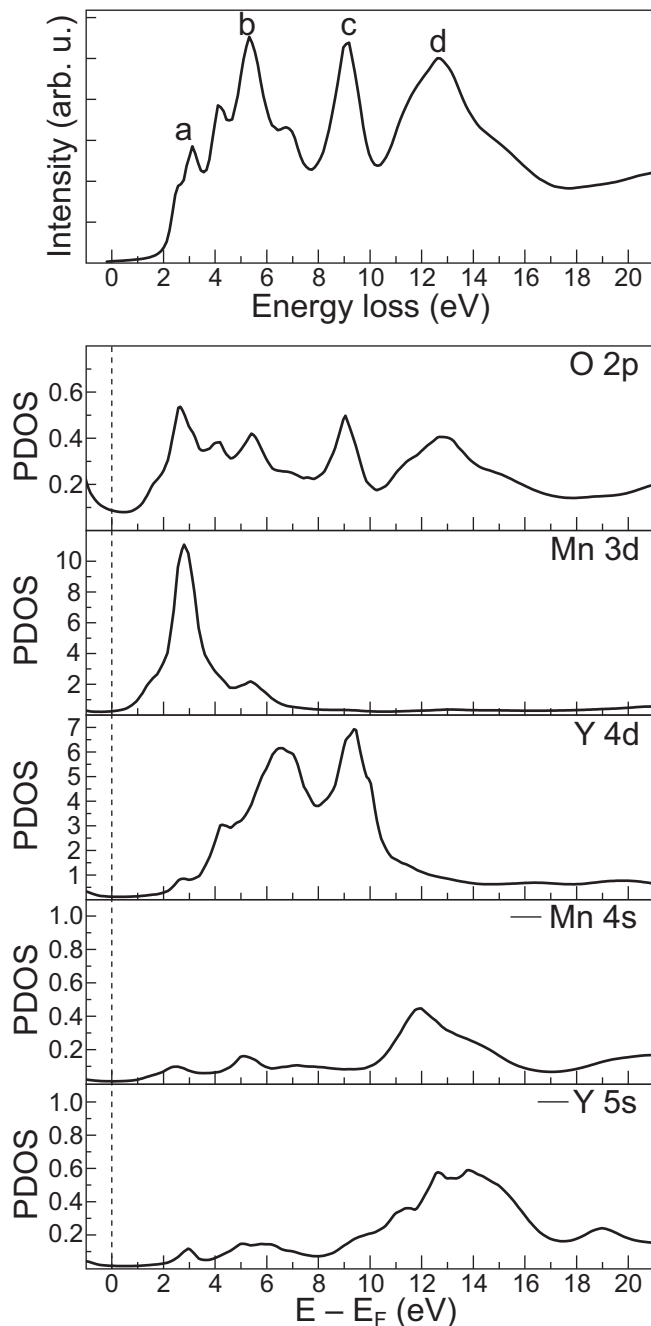


FIG. 6. Calculated O-*K* edge EEL spectrum and projected density of states (PDOS) of the ferroelectric YMO structure. The four main features, also observed in the EELS experimental data, are labeled *a*–*d*. Contributions of the different atomic orbitals for the O, Mn, and Y atomic species are given in the panels below.

#### IV. DISCUSSION

Our experimental data show that over several heating-cooling cycles, the intensity of the O-*K* preedge (peak *a*) progressively decreases until it disappears completely. This is a clear indication of the formation of oxygen vacancies [43,48,50,51]. In particular, the combination of the high temperatures used in the *in situ* experiment and the high-vacuum conditions of the TEM favors the loss of oxygen in

the YMO film. And indeed, previous studies reported that oxygen vacancies are likely to form in YMO at the planar O4 positions, since their formation energy was shown to be lowest at these positions [48,52]. Conversely, we have shown that significant and reproducible spectral changes occur at the O-*K* edge of a 14-u.c. YMO film across the phase transition over four heating-cooling cycles. Therefore, these changes are independent of the film oxygen concentration. Our calculations of the O-*K* edge and corresponding PDOS actually reveal that the observed changes in the peak *c*, although small, are due to a modification in the hybridization of the Y 4*d* with O 2*p* states, in agreement with previous reports [24,27]. This hybridization is highly anisotropic and occurs essentially between the empty Y  $d_z^2$  orbital and the populated  $p_z$  orbitals of the nearest oxygen ions along the *c*-axis polarization direction of the FE phase [53]. At the same time, the O 2*p* and Mn 3*d* states show some degree of hybridization, as revealed by the peak *b*, which is essentially the same in both FE and PE phases [53]. Thus, these *in situ* EELS data provide important information about the properties of the Y–O and Mn–O bonds in YMO and can be related to the real-space structural changes that occur during the phase transition.

In the ferroelectric phase, two Y1–O3 distances ( $\sim 2.33$  and  $\sim 3.38$  Å) and two Y2–O4 distances ( $\sim 2.45$  and  $\sim 3.25$  Å) are found due to the corrugation of the Y layer. At the same time, the Y–O1,2 bonds are shorter ( $\sim 2.28$  to  $\sim 2.32$  Å) [54]. These distances are indicated in Fig. 1(d). Across the phase transition, the Y–O bond lengths change, as evidenced by the HAADF-STEM images of Fig. 2(a). The bond distances for the high-temperature phase shown in Fig. 1(d) are estimated using the lattice expansion measured from the HAADF-STEM images. In the paraelectric phase, the distance between the Y ions and all planar oxygen ions (Op) is the same ( $\sim 2.94$  Å) and the distance between the Y ions and the apical oxygen ion (Oa) increases to  $\sim 2.40$  Å. In the ferroelectric phase, the shorter Y1–O3 bond is of the same order as the Y1–O1,2 and Y2–O1,2 bonds, which allows for the hybridization of the Y  $4d_z^2$  orbitals with O  $2p_z$  orbitals [55]. In contrast, in the paraelectric phase, where the Y layer is not corrugated, the Y–Op bonds are too far apart and have a purely ionic character with no significant hybridization of the O  $2p_z$  and Y  $4d_z^2$  orbitals, while the Y–Oa bonds have a covalent character that allows for this hybridization [20]. Consequently, the intensity of the peak *c* decreases in the paraelectric phase.

Our findings agree well with those of Cho *et al.* [27] and Kim *et al.* [56], who also identified partial Y 4*d*–O 2*p* rehybridization at the PE  $\rightarrow$  FE phase transition. They suggested that the condensation of the zone-boundary  $K_3$  mode coupled with the  $\Gamma_2^-$  mode arising at the PE  $\rightarrow$  FE phase transition, which give rise to two different Y–O interatomic distances along the *c*-axis polarization direction, is stabilized by hybridization at the shortest bonds. Further, our O-*K* edge and PDOS calculations are consistent with those of Deng *et al.* [49] and Cheng *et al.* [48], who systematically investigated the electronic and crystal structure modifications induced by oxygen vacancies in bulk YMO crystals. Their orbital-resolved DOS also suggests that the Y 4*d*–O 2*p* hybridization plays a role in driving improper ferroelectricity in YMO [49]. However, it is unlikely that the detected partial

rehybridization of the Y–O bond is the driving force for ferroelectricity in YMO. In fact, Kumagai *et al.* [33] investigated a variety of  $h$ -RMnO<sub>3</sub> ( $R$ = Sc, In, Lu, Tl, Y) compounds and concluded that in the improper ferroelectric hexagonal manganites, in contrast to proper ferroelectrics, stronger  $R$ –O covalency favors the paraelectric phase. Thus, as suggested by Song *et al.* [57], the emergence of a net polarization in the  $P6_3cm$  structure of YMO is enabled by the condensation of the polar  $\Gamma_2^-$  mode, which causes an additional displacement of the  $R$  sublattice with respect to the Mn–O layers.

Previous works have explored the phase transition in proper ferroelectrics by EELS [58,59]. Gallegos-Orozco *et al.* [59] and Bugnet *et al.* [58] characterized the PE-FE transition in the proper ferroelectric BaTiO<sub>3</sub> by low- and core-loss EELS. The spectral changes they observed were so subtle that only by comparison with *ab initio* density-functional theory calculations could they identify the small changes in the experimental spectra of the FE and PE phases. Nevertheless, similar to our findings, Bugnet *et al.* [58] showed that the near-edge structures of the O- $K$  edge are more sensitive to the structural distortions of the BaTiO<sub>3</sub> polymorphs than those of the  $3d$  transition-metal  $L_{3,2}$  edge. They observed a slight broadening of the O- $K$  preedge, originating from O  $2p$ -Ti  $3d$  hybridized states, with decreasing temperature and symmetry. Thus, the spectral changes that Bugnet *et al.* [58] probed were related to small distortions of the TiO<sub>6</sub> octahedra. Instead, the substantially larger changes detected at the O- $K$  edge of YMO are due to the large off-center displacements of the Y and in-plane O ions (O<sub>3,4</sub>) that allow Y  $4d_z^2$ -O  $2p_z$  hybridization in the FE phase. At the same time, the Mn ions remain near the center of their oxygen cages for both low- and high-temperature polymorphs, so that the O  $2p$ -Mn  $3d$  hybridization remains essentially unchanged. Thus, our results reveal a remarkably high sensitivity of the O- $K$  near-edge structures to the prominent structural distortions in improper ferroelectrics whose ferroelectricity emerges through coupling to a nonpolar lattice distortion and unveil a strategy to advance the understand-

ing of polymorphic phase transformations in this type of systems.

## V. CONCLUSION

The electronic structure of a 14-u.c. YMO epitaxial thin film was studied across the paraelectric-ferroelectric phase transition using *in situ* heating STEM-EELS. The experimental EELS data acquired above and below the Curie temperature are compared with calculations of the O- $K$  edge spectra and the corresponding PDOS of the ferroelectric phase. Thus, the observed changes in the EEL spectral features at the PE-FE phase transition are related to modifications in the Y  $4d$ -O  $2p$  hybridization. In particular, a weakening of the Y  $4d$ -O  $2p$  hybridization is detected for the paraelectric phase compared to the ferroelectric phase, as observed by a decrease in the intensity of the peak  $c$ . This is attributed to an increase in the length of the Y–O bonds between the Y ions and the planar O ions along the  $c$  axis. Upon cooling below the Curie temperature, the ferroelectric phase is restored and the enhanced hybridization of the Y  $4d_z^2$  orbitals with O  $2p_z$  orbitals is reestablished. Furthermore, the formation of oxygen vacancies over several heating-cooling cycles favored by the high-vacuum conditions of the TEM was also identified. As a result, the O- $K$  preedge (peak  $a$ ) vanishes. These modifications are independent of the spectral changes observed due to the PE-FE phase transition. Our results clarify some of the remaining uncertainties about the electronic structure of YMO at the PE-FE phase transition.

## ACKNOWLEDGMENTS

A.V., A.R.-C., and M.D.R. acknowledge support by the Swiss National Science Foundation (SNSF) under Project No. 200021\_175926. R.E. and M.D.R. acknowledge the financial support from the SNSF R'Equip Grant No. 206021\_189625. J.N. acknowledges support by the SNSF under Project No. P2EZP2\_195686. M.T. acknowledges support by the SNSF under Project No. 200021\_188414.

- 
- [1] S.-W. Cheong, SOS: Symmetry-operational similarity, *npj Quantum Mater.* **4**, 53 (2019).
  - [2] S. Gerardin and A. Paccagnella, Present and future non-volatile memories for space, *IEEE Trans. Nucl. Sci.* **57**, 3016 (2010).
  - [3] M. Müller, I. Efe, M. F. Sarott, E. Gradauskaite, and M. Trassin, Ferroelectric thin films for oxide electronics, *ACS Appl. Electron. Mater.* **5**, 1314 (2023).
  - [4] V. Dvořák, Improper ferroelectrics, *Ferroelectrics* **7**, 1 (1974).
  - [5] A. P. Levanyuk and D. G. Sannikov, Improper ferroelectrics, *Sov. Phys. Uspekhi* **17**, 199 (1974).
  - [6] C. J. Fennie and K. M. Rabe, Ferroelectric transition in YMnO<sub>3</sub> from first principles, *Phys. Rev. B* **72**, 100103(R) (2005).
  - [7] S.-W. Cheong and M. Mostovoy, Multiferroics: A magnetic twist for ferroelectricity, *Nat. Mater.* **6**, 13 (2007).
  - [8] N. Sai, C. J. Fennie, and A. A. Demkov, Absence of Critical Thickness in an Ultrathin Improper Ferroelectric Film, *Phys. Rev. Lett.* **102**, 107601 (2009).
  - [9] Z. J. Huang, Y. Cao, Y. Y. Sun, Y. Y. Xue, and C. W. Chu, Coupling between the ferroelectric and antiferromagnetic orders in YMnO<sub>3</sub>, *Phys. Rev. B* **56**, 2623 (1997).
  - [10] D. Meier, J. Seidel, A. Cano, K. Delaney, Y. Kumagai, M. Mostovoy, N. A. Spaldin, R. Ramesh, and M. Fiebig, Anisotropic conductance at improper ferroelectric domain walls, *Nat. Mater.* **11**, 284 (2012).
  - [11] Q. N. Meier *et al.*, Global Formation of Topological Defects in the Multiferroic Hexagonal Manganites, *Phys. Rev. X* **7**, 041014 (2017).
  - [12] S. M. Griffin, M. Lilienblum, K. T. Delaney, Y. Kumagai, M. Fiebig, and N. A. Spaldin, Scaling Behavior and Beyond Equilibrium in the Hexagonal Manganites, *Phys. Rev. X* **2**, 041022 (2012).
  - [13] Q. Zhang, G. Tan, L. Gu, Y. Yao, C. Jin, Y. Wang, X. Duan, and R. Yu, Direct observation of multiferroic vortex domains in YMnO<sub>3</sub>, *Sci. Rep.* **3**, 2741 (2013).



- [14] C. Becher *et al.*, Strain-induced coupling of electrical polarization and structural defects in SrMnO<sub>3</sub> films, *Nat. Nanotechnol.* **10**, 661 (2015).
- [15] S. H. Skjærvø, E. T. Wefring, S. K. Nesdal, N. H. Gaukås, G. H. Olsen, J. Glaum, T. Tybell, and S. M. Selbach, Interstitial oxygen as a source of P-type conductivity in hexagonal manganites, *Nat. Commun.* **7**, 13745 (2016).
- [16] S. Cheng *et al.*, Interface reconstruction with emerging charge ordering in hexagonal manganite, *Sci. Adv.* **4**, eaar4298 (2018).
- [17] M. E. Holtz, K. Shapovalov, J. A. Mundy, C. S. Chang, Z. Yan, E. Bourret, D. A. Muller, D. Meier, and A. Cano, Topological defects in hexagonal manganites: Inner structure and emergent electrostatics, *Nano Lett.* **17**, 5883 (2017).
- [18] Y. Kumagai and N. A. Spaldin, Structural domain walls in polar hexagonal manganites, *Nat. Commun.* **4**, 1540 (2013).
- [19] D. R. Småbråten, Q. N. Meier, S. H. Skjærvø, K. Inzani, D. Meier, and S. M. Selbach, Charged domain walls in improper ferroelectric hexagonal manganites and gallates, *Phys. Rev. Mater.* **2**, 114405 (2018).
- [20] B. B. Van Aken, T. T. M. Palstra, A. Filippetti, and N. A. Spaldin, The origin of ferroelectricity in magnetoelectric YMnO<sub>3</sub>, *Nat. Mater.* **3**, 164 (2004).
- [21] S. Artyukhin, K. T. Delaney, N. A. Spaldin, and M. Mostovoy, Landau theory of topological defects in multiferroic hexagonal manganites, *Nat. Mater.* **13**, 42 (2014).
- [22] T. A. Tyson, T. Wu, H. Y. Chen, J. Bai, K. H. Ahn, K. I. Pandya, S. B. Kim, and S.-W. Cheong, Measurements and ab initio molecular dynamics simulations of the high temperature ferroelectric transition in hexagonal RMnO<sub>3</sub>, *J. Appl. Phys.* **110**, 084116 (2011).
- [23] G. Nénert, M. Pollet, S. Marinell, G. R. Blake, A. Meetsma, and T. T. M. Palstra, Experimental evidence for an intermediate phase in the multiferroic YMnO<sub>3</sub>, *J. Phys.: Condens. Matter.* **19**, 466212 (2007).
- [24] J. Kim, K. C. Cho, Y. M. Koo, K. P. Hong, and N. Shin, Y–O hybridization in the ferroelectric transition of YMnO<sub>3</sub>, *Appl. Phys. Lett.* **95**, 132901 (2009).
- [25] T. Katsufuji *et al.*, Crystal structure and magnetic properties of Hexagonal RMnO<sub>3</sub> = Y, Lu, and Sc, *Phys. Rev. B* **66**, 134434 (2002).
- [26] A. S. Gibbs, K. S. Knight, and P. Lightfoot, High-temperature phase transitions of hexagonal YMnO<sub>3</sub>, *Phys. Rev. B* **83**, 094111 (2011).
- [27] D.-Y. Cho, J.-Y. Kim, B.-G. Park, K.-J. Rho, J.-H. Park, H.-J. Noh, B.J. Kim, S.-J. Oh, H.-M. Park, J.-S. Ahn, H. Ishibashi, S.-W. Cheong, J. H. Lee, P. Murugavel, T. W. Noh, A. Tanaka, and T. Jo, Ferroelectricity Driven by Y *d<sup>0</sup>*-Ness with Rehybridization in YMnO<sub>3</sub>, *Phys. Rev. Lett.* **98**, 217601 (2007).
- [28] M. Lilienblum, T. Lottermoser, S. Manz, S. M. Selbach, A. Cano, and M. Fiebig, Ferroelectricity in the multiferroic hexagonal manganites, *Nat. Phys.* **11**, 1070 (2015).
- [29] S. H. Skjærvø, Q. N. Meier, M. Feygenson, N. A. Spaldin, S. J. L. Billinge, E. S. Bozin, and S. M. Selbach, Unconventional Continuous Structural Disorder at the Order-Disorder Phase Transition in the Hexagonal Manganites, *Phys. Rev. X* **9**, 031001 (2019).
- [30] A. Cano, Hidden order in hexagonal RMnO<sub>3</sub> multiferroics (R = Dy–Lu, In, Y, and Sc), *Phys. Rev. B* **89**, 214107 (2014).
- [31] R. I. Thomson, T. Chatterji, C. J. Howard, T. T. M. Palstra, and M. A. Carpenter, Elastic anomalies associated with structural and magnetic phase transitions in single crystal hexagonal YMnO<sub>3</sub>, *J. Phys.: Condens. Matter* **26**, 045901 (2014).
- [32] J. Nordlander, M. Campanini, M. D. Rossell, R. Erni, Q. N. Meier, A. Cano, N. A. Spaldin, M. Fiebig, and M. Trassin, The ultrathin limit of improper ferroelectricity, *Nat. Commun.* **10**, 5591 (2019).
- [33] Y. Kumagai, A. A. Belik, M. Lilienblum, N. Leo, M. Fiebig, and N. A. Spaldin, Observation of persistent centrosymmetry in the hexagonal manganite family, *Phys. Rev. B* **85**, 174422 (2012).
- [34] J. Nordlander, M. D. Rossell, M. Campanini, M. Fiebig, and M. Trassin, Epitaxial integration of improper ferroelectric hexagonal YMnO<sub>3</sub> thin films in heterostructures, *Phys. Rev. Mater.* **4**, 124403 (2020).
- [35] F. Kahl, V. Gerheim, M. Linck, H. Müller, R. Schillinger, and S. Uhlemann, Test and Characterization of a New Post-Column Imaging Energy Filter, *Adv. Imaging Electron Phys.* **212**, 35 (2019).
- [36] A. Ruiz-Caridad, R. Erni, A. Vogel, and M. D. Rossell, Applications of a novel electron energy filter combined with a hybrid-pixel direct electron detector for the analysis of functional oxides by STEM/EELS and energy-filtered imaging, *Micron* **160**, 103331 (2022).
- [37] B. Plotkin-Swing *et al.*, Hybrid pixel direct detector for electron energy loss spectroscopy, *Ultramicroscopy* **217**, 113067 (2020).
- [38] L. Jones, H. Yang, T. J. Pennycook, M. S. J. J. Marshall, S. Van Aert, N. D. Browning, M. R. Castell, and P. D. Nellist, Smart Align—a new tool for robust non-rigid registration of scanning microscope data, *Adv. Struct. Chem. Imaging* **1**, 8 (2015).
- [39] J. J. Rehr, J. J. Kas, F. D. Vila, M. P. Prange, and K. Jorissen, Parameter-free calculations of x-ray spectra with FEFF9, *Phys. Chem. Chem. Phys.* **12**, 5503 (2010).
- [40] L. Hedin and S. Lundqvist, Effects of electron-electron and electron-phonon interactions on the one-electron states of solids, *Solid State Phys.* **23**, 1 (1970).
- [41] M. S. Moreno, K. Jorissen, and J. J. Rehr, Practical aspects of electron energy-loss spectroscopy (EELS) calculations using FEFF8, *Micron* **38**, 1 (2007).
- [42] A. Vogel, A. Ruiz-Caridad, J. Nordlander, M. F. Sarott, Q. N. Meier, R. Erni, N. A. Spaldin, M. Trassin, and M. D. Rossell, Origin of the critical thickness in improper ferroelectric thin films, *ACS Appl. Mater. Interfaces* **15**, 18482 (2023).
- [43] M. Varela, M. P. Oxley, W. Luo, J. Tao, M. Watanabe, A. R. Lupini, S. T. Pantelides, and S. J. Pennycook, Atomic-resolution imaging of oxidation states in manganites, *Phys. Rev. B* **79**, 085117 (2009).
- [44] H. K. Schmid and W. Mader, Oxidation states of Mn and Fe in various compound oxide systems, *Micron* **37**, 426 (2006).
- [45] T. Riedl, T. Gemming, and K. Wetzig, Extraction of EELS white-line intensities of manganese compounds: Methods, accuracy, and valence sensitivity, *Ultramicroscopy* **106**, 284 (2006).
- [46] K. Asokan, C. L. Dong, C. W. Bao, H. M. Tsai, J. W. Chiou, C. L. Chang, W. F. Pong, P. Duran, C. Moure, and O. Peña, Electronic structures of hexagonal manganites HoMnO<sub>3</sub> studied by x-ray absorption near-edge structure, in *Proceedings of the Synchrotron Radiation Instrumentation: Ninth International Conference on Synchrotron Radiation Instrumentation*, AIP Conf. Proc. No. 879 (AIP, Daegu, South Korea, 2007), pp. 1659–1662.



- [47] K. Asokan *et al.*, Effect of Co, Ni, and Cu substitution on the electronic structure of hexagonal YMnO<sub>3</sub> studied by x-ray absorption spectroscopy, *Appl. Phys. Lett.* **95**, 131901 (2009).
- [48] S. Cheng, M. Li, Q. Meng, W. Duan, Y. G. Zhao, X. F. Sun, Y. Zhu, and J. Zhu, Electronic and crystal structure changes induced by in-plane oxygen vacancies in multiferroic YMnO<sub>3</sub>, *Phys. Rev. B* **93**, 054409 (2016).
- [49] S. Deng, S. Cheng, C. Xu, B. Ge, X. Sun, R. Yu, W. Duan, and J. Zhu, Atomic mechanism of hybridization-dependent surface reconstruction with tailored functionality in hexagonal multiferroics, *ACS Appl. Mater. Interfaces* **9**, 27322 (2017).
- [50] P. Agrawal, J. Guo, P. Yu, C. Hébert, D. Passerone, R. Erni, and M. D. Rossell, Strain-driven oxygen deficiency in multiferroic SrMnO<sub>3</sub> thin films, *Phys. Rev. B* **94**, 104101 (2016).
- [51] U. Aschauer, R. Pfenninger, S. M. Selbach, T. Grande, and N. A. Spaldin, Strain-controlled oxygen vacancy formation and ordering in CaMnO<sub>3</sub>, *Phys. Rev. B* **88**, 054111 (2013).
- [52] S. H. Skjærvø, D. R. Småbråten, N. A. Spaldin, T. Tybell, and S. M. Selbach, Oxygen vacancies in the bulk and at neutral domain walls in hexagonal YMnO<sub>3</sub>, *Phys. Rev. B* **98**, 184102 (2018).
- [53] W. Sotero, A. F. Lima, and M. V. Lalic, Analysis of the Mn–O and Y–O bonds in paraelectric and ferroelectric phase of magnetoelectric YMnO<sub>3</sub> from the first principles calculations, *J. Alloys Compd.* **649**, 285 (2015).
- [54] B. B. van Aken, A. Meetsma, and T. T. M. Palstra, Hexagonal YMnO<sub>3</sub>, *Acta Crystallogr. Sect. C Cryst. Struct. Commun.* **C57**, 230 (2001).
- [55] A. M. Sousa, W. S. Coutinho, A. F. Lima, and M. V. Lalic, Structural, bonding, and electronic properties of the hexagonal ferroelectric and paraelectric phases of LuMnO<sub>3</sub> compound: A density functional theory study, *J. Chem. Phys.* **142**, 074703 (2015).
- [56] D. J. Kim, J. Y. Jo, T. H. Kim, S. M. Yang, B. Chen, Y. S. Kim, and T. W. Noh, Observation of inhomogeneous domain nucleation in epitaxial Pb(Zr,Ti)O<sub>3</sub> capacitors, *Appl. Phys. Lett.* **91**, 132903 (2007).
- [57] S. Song, J.-H. Lee, and H. M. Jang, Mode coupling between nonpolar and polar phonons as the origin of improper ferroelectricity in hexagonal LuMnO<sub>3</sub>, *J. Mater. Chem. C* **2**, 4126 (2014).
- [58] M. Bugnet, G. Radtke, S. Y. Woo, G.-Z. Zhu, and G. A. Botton, Temperature-dependent high energy-resolution EELS of ferroelectric and paraelectric BaTiO<sub>3</sub> phases, *Phys. Rev. B* **93**, 020102(R) (2016).
- [59] V. Gallegos-Orozco, R. Martínez-Sánchez, and F. Espinosa-Magaña, In situ characterization of the ferroelectric transition in BaTiO<sub>3</sub> by EELS and comparison with ab initio methods, *Phys. Rev. B* **77**, 045128 (2008).